



A simplified depth-averaged debris flow model with Herschel-Bulkley rheology for tracking density evolution: a finite volume formulation

Dong Hun Kang¹ · Moonhyun Hong¹ · Sangseom Jeong¹

Received: 2 September 2020 / Accepted: 13 March 2021 / Published online: 13 May 2021
© Springer-Verlag GmbH Germany, part of Springer Nature 2021

Abstract

A two-phase depth-averaged debris flow model simplified by momentum equations is presented to solve the tracking of density evolution and simulate high-velocity impact problems. In the model, the Herschel-Bulkley rheology is used to describe the internal and basal frictions in the debris flow, and the treatments of complex terrains and entrainments are also included. To solve the debris flow model numerically, a relevant finite volume formulation including the Harten-Lax-van Leer-Contact (HLLC) scheme is introduced to solve the conservation equation with a debris interface. A circular dam-break, a dam-break of non-Newtonian fluid, and multiple debris flow cases are carried out based on the proposed model to validate the shock-capturing capability, the numerical isotropy, the model accuracy, and the mass conservation. These results indicate that the implemented schemes can produce sufficient numerical stability and accuracy for the debris flow problem. Finally, the debris flow of various rheological properties is systematically simulated, and how the debris rheology affects debris flow behavior is discussed.

Keywords Depth-averaged debris flow model · Herschel-Bulkley rheology · Harten-Lax-van Leer-Contact (HLLC) scheme

Introduction

Large-mass and high-velocity debris flows can be fatal to human society and infrastructures. In particular, the increase in the frequency and intensity of torrential rains caused by global climate change has induced debris flows in the mountains in urban areas (García-Delgado et al. 2019; Jeong et al. 2015). Solving these dynamic problems with extremely large deformations over a short event time is slightly different from traditional problems in geotechnical engineering. It is highly difficult to reproduce debris flows in the field, so lab- or large-scale experiments or numerical simulations are usually carried out to better understand the mechanisms and assess the risks (Chen and Lee 2000; Parsons et al. 2001; Crosta et al. 2009; Iverson et al. 2010, 2011). In South Korea, the real-scale debris flow experiment with terrestrial LiDAR was also attempted to figure out the debris flow mechanisms (Won et al. 2016).

When numerically simulating debris flows, many numerical models are usually based on the Savage-Hutter theory (Savage and Hutter 1989; Iverson 1997; Yavari-Ramshe et al. 2015). Their governing equations take the form of shallow water equations coupled with assumptions that include the incompressibility of materials, a small topology curvature, Coulomb frictional resistance, lateral pressure from the earth pressure coefficient, and a small horizontal momentum dissipation (Hutter et al. 2005). These flow models have to consider constant parameters such as the lateral earth pressure coefficient and the friction angle, which are usually acquired by independent experiments. However, these models are insufficient for reflecting the genuine behaviors of the debris mixture. Previous studies have proposed an effective stress-dependent frictional resistance (Iverson 1997), a μ -parametrization model (Pouliquen and Forterre 2002), a thermo-pore-mechanical model (Vardoulakis 2000), and the velocity-dependent friction law (Liu et al. 2016). In the dilatancy model, Iverson and George (2014) suggested that the pore water pressure induced by a volumetric change of debris mixture can alter the effective stress and corresponding friction resistance. In the μ -parametrization model, the friction coefficient $\mu (= \tan \delta)$ is considered a function of the non-dimensional inertial number. In the thermo-pore-mechanical model, the

✉ Sangseom Jeong
soj9081@yonsei.ac.kr

¹ School of Civil and Environmental Engineering, Yonsei University, Seoul 03722, South Korea

pore pressure generated by frictional heating alters the frictional resistance at the interface between the debris flow and basal surface. In the velocity-weakening friction model, the friction coefficient μ is interpolated between static and peak friction coefficients by the velocity magnitude.

Some studies have attempted to use a rheological model for non-Newtonian fluids or turbulent flows in shallow water equations to represent debris mixture behavior (Laigle and Coussot 1997; Zanuttigh and Lamberti 2004; Medina et al. 2008; Hong et al. 2019). The rheological model is more flexible in representing the velocity-dependent resistance than the Coulomb friction model. Additionally, previous studies have reported that Coulomb frictional resistance from constant bed friction could be insufficient to dampen debris velocity (Hutter and Greve 1993; Hutter et al. 2005). However, the viscous resistance in the rheological model could be much lower than the Coulomb frictional resistance when the debris flow has some thickness (Iverson 2003), and the estimation of rheological properties in debris mixtures has been less studied than in the Coulomb friction model. Some studies have attempted to estimate the rheological properties of debris mixtures by back analysis (Whipple 1997; Hürlimann et al. 2008). However, a systematic study on overall debris behavior according to various rheological properties is still necessary to verify the potential applicability of the rheological model.

One of the most difficult problems is to measure the rheological properties of the debris flow on the sediment characteristics, let alone the non-Newtonian fluids. The rheological properties of the debris material could be sensitive for solid volume fraction, particle sizes and shapes, etc. (Kaitna et al. 2007; Scotto Di Santolo et al. 2010; Pellegrino and Schippa 2018). Moreover, for a large-particulate debris mixture, conventional small-scale rheometers may be inapplicable and a large-scale rheometer specially designed for the debris should be used (Schatzmann et al. 2009; Pellegrino et al. 2016). The entrainment of basal sediment by the debris is a common process and can cause the change of the solid fraction and corresponding rheological properties of the debris. Also, the mixture density or solid fraction can vary when multiple debris flow with different densities merge at a confluence. Therefore, it is necessary to track the spatial distribution of the solid fraction at least to more realistically reflect the debris rheology in the numerical simulation. However, most previous numerical studies have used single-phase models that assume a constant mixture density (Chen and Lee 2000; Mangeney et al. 2007; Hong et al. 2019).

A few studies have recently suggested two-phase models for debris flows that contain continuity and momentum equations for both the solid and fluid phases (Pudasaini 2012; Li et al. 2018; Pastor et al. 2018). These two-phase models have a high potential to describe debris flow behaviors more realistically and overcome the limitations of current single-phase

models. However, a theoretical basis with experimental evidence on the fluid-solid interactions employed in these two-phase models is still insufficient, and the models require greater computational effort and more input parameters than single-phase models.

To solve the shallow water equations for debris flows, many numerical studies have used the smoothed particle hydrodynamics (SPH) method and the finite volume method (FVM) (Xia et al. 2013; Yavari-Ramshe et al. 2015; Wang et al. 2016; Xia and Liang 2018; Han et al. 2019). SPH is a meshless and full Lagrangian-type approach that solves the individual dynamics of fictitious fluid particles by using Newton's second law. The fluid-fluid and fluid-solid interactions are applied to the particles by volume averaging kernel functions that are macroscopically recovered by shallow water equations. However, SPH requires a sufficient number of particles to obtain an accurate solution, and the computational cost rapidly increases as the number of particles increases. Unlike SPH, the FVM is a mesh-based and Eulerian-type approach based on a divergence theorem that is specialized for computational fluid dynamics. Although SPH is flexible and can be recovered by shallow water equations, the numerical solutions obtained by SPH weakly and asymptotically satisfy the shallow water equations. In contrast, the FVM for debris flows requires sophisticated numerical treatments such as flux difference splitting schemes and can more strictly and accurately produce discontinuous solutions for shallow water equations.

This paper presents a simplified depth-averaged debris flow model for tracking density evolution. The developed model uses Herschel-Bulkley rheology in internal and basal frictions and considers complex terrains and entrainments. In particular, the interaction between solid-fluid phases in the mixture is ignored. A finite volume formulation of the proposed model is presented with relevant numerical schemes to obtain stable and accurate solutions. This work then validates dam-break and multiple debris flow simulations. In addition, the effect of debris rheology is discussed through a parametric study of a United States Geological Survey (USGS) experimental domain.

Methodology

Governing equations

The governing equations derived by depth-averaging the Navier-Stokes equations can facilitate debris flow simulations at a large scale by reducing the computational cost compared to full-scale 3D simulations. The continuity equations for the mixture and solid phases and the momentum equations of the mixture phase for x - and y -axes are given as

$$\frac{\partial h\rho}{\partial t} + \frac{\partial}{\partial x}(h\rho v_x) + \frac{\partial}{\partial y}(h\rho v_y) = -\rho_b \frac{\partial z_b}{\partial t} \tag{1}$$

$$\frac{\partial hc_s}{\partial t} + \frac{\partial}{\partial x}(hc_s v_{s,x}) + \frac{\partial}{\partial y}(hc_s v_{s,y}) = -c_{bs} \frac{\partial z_b}{\partial t} \tag{2}$$

$$\begin{aligned} \frac{\partial h\rho v_x}{\partial t} + \frac{\partial h\rho\alpha_m v_x v_x}{\partial x} + \frac{\partial h\rho\alpha_m v_y v_x}{\partial y} \\ = -\frac{\partial h\bar{p}}{\partial x} + \frac{\partial h\bar{\tau}_{xx}}{\partial x} + \frac{\partial h\bar{\tau}_{yx}}{\partial y} - p_b \frac{\partial z_b}{\partial x} + \omega\tau_b t_{b,x} \end{aligned} \tag{3}$$

$$\begin{aligned} \frac{\partial h\rho v_y}{\partial t} + \frac{\partial h\rho\alpha_m v_x v_y}{\partial x} + \frac{\partial h\rho\alpha_m v_y v_y}{\partial y} \\ = -\frac{\partial h\bar{p}}{\partial y} + \frac{\partial h\bar{\tau}_{xy}}{\partial x} + \frac{\partial h\bar{\tau}_{yy}}{\partial y} - p_b \frac{\partial z_b}{\partial y} + \omega\tau_b t_{b,y} \end{aligned} \tag{4}$$

where h , ρ , and c_s are the debris height, mixture density, and solid volume fraction, respectively. v_k and $v_{s,k}$ are the k -axis components of depth-averaged velocity for the mixture and solid phases, respectively. ρ_b and c_{bs} are the mixture density and solid volume fraction of an entrained basal sediment. z_b is the surface level of basal sediment. α_m is a momentum correction factor. $\bar{\tau}_{ij}$ is the depth-averaged shear stress. \bar{p} and p_b are depth-averaged and basal pressures, respectively. τ_b is the basal friction stress. $t_{b,k}$ is a direction vector of basal friction. ω is a ratio of the basal surface area to its projection area onto the x - y plane, which can be written as

$$\omega = \sqrt{\left(\frac{\partial z_b}{\partial x}\right)^2 + \left(\frac{\partial z_b}{\partial y}\right)^2 + 1} \tag{5}$$

The derivation of the governing equation is provided in the [Supplementary material](#) in detail. This study assumes that the velocity difference between solid and water phases is sufficiently small and that this assumption is more definite in a high-velocity regime. Therefore, only the mixture velocity is considered as $v_k \approx v_{s,k}$. By assuming a linear distribution of the pressure along the z -direction and the flow velocity parallel to the basal surface, the bulk pressure p and the apparent gravitational acceleration \hat{g} are given as (Xia and Liang 2018)

$$p = \rho\hat{g}(z_b + h - z) \tag{6}$$

$$\hat{g} = \frac{1}{\omega^2} [g + \mathbf{v}^T \mathbf{H} \mathbf{v}] \tag{7}$$

in which

$$\mathbf{v} = \begin{bmatrix} v_x \\ v_y \end{bmatrix} \quad \text{and} \quad \mathbf{H} = \begin{bmatrix} \frac{\partial^2 z_b}{\partial x^2} & \frac{\partial^2 z_b}{\partial x \partial y} \\ \frac{\partial^2 z_b}{\partial x \partial y} & \frac{\partial^2 z_b}{\partial y^2} \end{bmatrix} \tag{8}$$

where \mathbf{H} is the Hessian matrix of the basal surface elevation.

The z -axis component of depth-averaged velocity and the direction vector of basal friction are expressed as

$$v_z = v_x \frac{\partial z_b}{\partial x} + v_y \frac{\partial z_b}{\partial y} \tag{9}$$

$$t_{b,k} = -\frac{v_k}{\sqrt{v_x^2 + v_y^2 + v_z^2}} \tag{10}$$

In open channel flow, the velocity profile along the z -direction is necessary to calculate basal viscous friction and is commonly known to be a function of the rheological model, velocity magnitude, and basal surface roughness, but it remains unclarified in the debris flow. For calculating basal friction, previous studies of shallow water equation simulations have used the Manning equation, which is an empirical equation for a relationship among an averaged velocity, a flow area, a channel slope, and a basal roughness (Xia et al. 2017; Hou et al. 2018). However, Manning’s roughness coefficient was originally given for water, so the coefficient is typically corrected depending on the debris rheology. Instead, this study assumes that the debris flow follows the nonlinear velocity profile model proposed by Johnson et al. (2012) as

$$u_k = (2-\alpha) \left(1 - \left(1 - \frac{z-z_b}{h} \right)^{\frac{1}{1-\alpha}} \right) v_k \tag{11}$$

where u_k is the debris velocity in the 3D space reproduced using a nonlinear velocity profile model and a depth-averaged velocity v_k . α is a profile shape parameter ranging between 0 to 1 and is herein set as 0.7. As α approaches 1, the velocity profile moves to a plug-like profile from a linear-like profile. The momentum correction factor and the basal friction stress of the rheological materials can be given as

$$\alpha_m = \frac{4-2\alpha}{3-\alpha} \tag{12}$$

$$\tau_b = \mu \frac{2-\alpha}{(1-\alpha)} \frac{\sqrt{v_x^2 + v_y^2 + v_z^2}}{h} \tag{13}$$

where μ is the debris viscosity.

This study uses the Herschel-Bulkley model for the rheology of debris flow as

$$\mu = \min([\tau_y + k_0 \gamma^n] \gamma^{-1}, \mu_{\max}) \tag{14}$$

where τ_y is the yield stress, γ is the magnitude of the shear rate, k_0 is a consistency index, n is a flow index, and μ_{\max} is the maximum viscosity that prevents infinitely high viscosity when the shear rate approaches zero.

The depth-averaged shear strain and stress tensors are approximated as

$$\bar{\gamma}_{ij} \approx \frac{1}{2} (\partial_i v_j + \partial_j v_i) \quad \text{for } i, j = x, y, \text{ and } z \tag{15}$$

$$\bar{\tau}_{ij} = \mu\bar{\gamma}_{ij} \quad \text{for } i, j = x \text{ and } y \tag{16}$$

The x - and y -directional derivatives of the depth-averaged velocity in Eq. (16) are approximated by the central difference scheme. The z -directional derivative is assumed as

$$\frac{\partial v_k}{\partial z} \approx \frac{u_k|_{z_b+h} - u_k|_{z_b}}{h} = (2-\alpha)\frac{v_k}{h} \tag{17}$$

This study uses the dynamic equilibrium approach for the entrainment of basal sediment proposed by Fraccarollo and Capart (2002) and Medina et al. (2008). The entrainment rate is given as

$$\frac{\partial z_b}{\partial t} = -\frac{\tau_b - \sigma'_b \tan \phi_{bs} - c_{bs}}{\rho \sqrt{v_x^2 + v_y^2 + v_z^2}} \tag{18}$$

where ϕ_{bs} and c_{bs} are the internal friction angle and cohesion of the basal sediment, respectively.

By implementing a time integration of Eq. (18), we can obtain the erosion position z_e , which becomes the new basal surface level after the entrainment as

$$z_b(t + \Delta t) = z_e = z_b(t) + \int_t^{t+\Delta t} \frac{\partial z_b}{\partial t} dt \tag{19}$$

Our model tracks the local volume fraction of the solid phase, and the debris flow is assumed to be fully saturated regardless of the minimum void ratio of the soil particles. In this sense, to avoid a violation of mass conservation when the mass of eroded sediment at an unsaturated state is mixed with debris at a fully saturated state, the density of the eroded basal sediment ρ_{bs} should be evaluated as

$$\rho_{bs} = \frac{1}{z_b - z_e} \int_{z_e}^{z_b} \rho_b(z) dz = \frac{\rho_w G_s}{1 + e} + \frac{\rho_w}{z_b - z_e} \int_{z_e}^{z_b} \theta(z) dz \tag{20}$$

where ρ_b and θ are the sediment density and the volumetric water content below the basal surface, respectively. G_s is the specific gravity of a soil. ρ_w is the density of water.

Model implementation

The physical and mathematical properties of the shallow water equations are analogous to the shock propagation in a compressible fluid in terms of the constant values around one discontinuous interface. This advection-dominant flow is sometimes considered a Riemann problem and is difficult to solve by the traditional numerical differencing schemes used for partial differential equations with a smooth solution. To solve the Riemann problem in computational fluid dynamics, flux-difference splitting or flux-vector splitting schemes are usually implemented. This study also implements the Harten-Lax-van Leer-Contact (HLLC) approximate Riemann solver, which is a powerful flux-difference splitting scheme (Toro 2002).

The governing equation can be rewritten in vector form as

$$\frac{\partial \mathbf{U}}{\partial t} + \frac{\partial \mathbf{F}_x(\mathbf{U})}{\partial x} + \frac{\partial \mathbf{F}_y(\mathbf{U})}{\partial y} = \frac{\partial \mathbf{T}_x}{\partial x} + \frac{\partial \mathbf{T}_y}{\partial y} + \mathbf{S}_s + \mathbf{S}_d \tag{21}$$

where \mathbf{U} is a vector of conserved variables. $\mathbf{F}_x(\mathbf{U})$ and $\mathbf{F}_y(\mathbf{U})$ are advection vectors of \mathbf{U} for the x - and y -axes. \mathbf{T}_x and \mathbf{T}_y are momentum dissipation vectors for the x - and y -axes. \mathbf{S}_s is a mass and momentum source vector, and \mathbf{S}_d is a drag vector.

Those vector terms are given by

$$\begin{aligned} \mathbf{U} &= \left\{ \begin{array}{l} h\rho \\ hc_s \\ h\rho v_x \\ h\rho v_y \end{array} \right\}, \mathbf{F}_x = \left\{ \begin{array}{l} h\rho v_x \\ hc_s v_x \\ h\rho \alpha_m v_x v_x + \frac{1}{2} \partial_x \rho \widehat{g} h^2 \\ h\rho \alpha_m v_y v_x \end{array} \right\}, \mathbf{F}_y = \left\{ \begin{array}{l} h\rho v_y \\ hc_s v_y \\ h\rho \alpha_m v_x v_y \\ h\rho \alpha_m v_y v_y + \frac{1}{2} \partial_y \rho \widehat{g} h^2 \end{array} \right\} \\ \mathbf{T}_x &= \left\{ \begin{array}{l} 0 \\ 0 \\ h\mu \bar{\gamma}_{xx} \\ h\mu \bar{\gamma}_{xy} \end{array} \right\}, \mathbf{T}_y = \left\{ \begin{array}{l} 0 \\ 0 \\ h\mu \bar{\gamma}_{yx} \\ h\mu \bar{\gamma}_{yy} \end{array} \right\}, \mathbf{S}_s = \left\{ \begin{array}{l} -\rho_b \partial_t z_b \\ -c_{bs} \partial_t z_b \\ -2\bar{p} \partial_x z_b \\ -2\bar{p} \partial_y z_b \end{array} \right\}, \mathbf{S}_d = \left\{ \begin{array}{l} 0 \\ 0 \\ \omega \tau_b t_{b,x} \\ \omega \tau_b t_{b,y} \end{array} \right\} \end{aligned} \tag{22}$$

The semi-discrete form for the volume integration of Eq. (21) for a rectangular cell at (x_i, y_j) can be expressed by

$$\begin{aligned} \frac{\partial U_{i,j}}{\partial t} &= \frac{1}{dA} \left(\Delta y F_x^{i-\frac{1}{2},j} - \Delta y F_x^{i+\frac{1}{2},j} + \Delta x F_y^{i,j-\frac{1}{2}} - \Delta x F_y^{i,j+\frac{1}{2}} \right) \\ &+ \frac{1}{dA} \left(\Delta y T_x^{i-\frac{1}{2},j} - \Delta y T_x^{i+\frac{1}{2},j} + \Delta x T_y^{i,j-\frac{1}{2}} - \Delta x T_y^{i,j+\frac{1}{2}} \right) + S_s^{i,j} + S_d^{i,j} \end{aligned} \tag{23}$$

where Δx and Δy are the cell edge sizes, dA is the cell area (i.e., $\Delta x \Delta y$). $\mathbf{F}_x^{i\pm\frac{1}{2},j}$ are advection fluxes passing through cell faces at $(x_i \pm \frac{1}{2} \Delta x, y_j)$. Similarly, $\mathbf{F}_y^{i,j\pm\frac{1}{2}}$ are advection fluxes passing through cell faces at $(x_i, y_j \pm \frac{1}{2} \Delta y)$.

In the HLLC scheme, the cell-faced values of the conserved variables and the advection fluxes are calculated by considering the three characteristic wave speeds as

$$\mathbf{U}^{i+\frac{1}{2},j} = \begin{cases} \mathbf{U}_M^{i+\frac{1}{2},j} & 0 \leq S^{i+\frac{1}{2},j} \\ \mathbf{U}_M^{i+\frac{1}{2},j} & S^{i+\frac{1}{2},j} \leq 0 \leq S_M^{i+\frac{1}{2},j} \\ \mathbf{U}_M^{i+\frac{1}{2},j} & S_M^{i+\frac{1}{2},j} \leq 0 \leq S^{i+\frac{1}{2},j} \\ \mathbf{U}_M^{i+\frac{1}{2},j} & S^{i+\frac{1}{2},j} < 0 \end{cases} \quad (24)$$

and

$$\mathbf{F}^{i+\frac{1}{2},j} = \begin{cases} \mathbf{F}_M^{i+\frac{1}{2},j} & 0 \leq S^{i+\frac{1}{2},j} \\ \mathbf{F}_M^{i+\frac{1}{2},j} & S^{i+\frac{1}{2},j} \leq 0 \leq S_M^{i+\frac{1}{2},j} \\ \mathbf{F}_M^{i+\frac{1}{2},j} & S_M^{i+\frac{1}{2},j} \leq 0 \leq S^{i+\frac{1}{2},j} \\ \mathbf{F}_M^{i+\frac{1}{2},j} & S^{i+\frac{1}{2},j} < 0 \end{cases} \quad (25)$$

where $S^{i+\frac{1}{2},j}$, $S_M^{i+\frac{1}{2},j}$, and $S^{i+\frac{1}{2},j}$ are the characteristic wave speeds of the left, middle, and right regions of a cell face at $(x_i + \frac{1}{2} \Delta x, y_j)$. $\mathbf{U}^{i+\frac{1}{2},j}$ and $\mathbf{F}^{i+\frac{1}{2},j}$ are conservative variables and advection fluxes extrapolated by using a flux limiter at the left and right sides of a cell face. $\mathbf{U}_M^{i+\frac{1}{2},j}$ and $\mathbf{F}_M^{i+\frac{1}{2},j}$ are conservative variables and advection fluxes at the left and right middle regions of a cell face.

The interface values of a quantity ξ at the left and right sides of a cell face at $(x_i + \frac{1}{2} \Delta x, y_j)$ can be extrapolated as

$$\xi^{i+\frac{1}{2},j} = \xi^{i,j} + \frac{\Delta x}{2} \Psi(r^{i,j}) \frac{\partial \xi}{\partial x} \Big|_{i,j}^{\text{up}} \quad (26)$$

$$\xi^{i+\frac{1}{2},j} = \xi^{i+1,j} - \frac{\Delta x}{2} \Psi(r^{i+1,j}) \frac{\partial \xi}{\partial x} \Big|_{i+1,j}^{\text{up}} \quad (27)$$

where $r^{i,j}$ is a ratio of successive gradients, Ψ is a flux limiter function, and $\partial_x \xi|_{i+1,j}^{\text{up}}$ is an x -directional unlimited gradient of a quantity ζ , calculated by the upwind difference scheme.

The ratio of successive gradients is given as

$$r^{i,j} = \frac{\xi^{\text{up}} - \xi^{i,j}}{\xi^{i,j} - \xi^{\text{down}}} \quad (28)$$

where ξ^{up} and ξ^{down} are upstream and downstream cell-centered values, respectively.

This study uses the van Leer limiter function as

$$\Psi(r) = \frac{r + |r|}{1 + |r|} \quad (29)$$

The basal surface level at a cell face $z_b^{i+\frac{1}{2},j}$ is obtained by the hydrostatic reconstruction method proposed by Audusse et al. (2004) to avoid a negative debris height as

$$z_b^{i+\frac{1}{2},j} = \max\left([z_b + h]^{i+\frac{1}{2},j} - h^{i+\frac{1}{2},j}, [z_b + h]^{i+\frac{1}{2},j} - h^{i+\frac{1}{2},j}\right) \quad (30)$$

where $h^{i+\frac{1}{2},j}$ are calculated by Eqs. (26) and (27).

After the calculation of $z_b^{i+\frac{1}{2},j}$, the interface values of debris height $h^{i+\frac{1}{2},j}$ are recalculated by

$$h^{i+\frac{1}{2},j} = \max\left(0, [z_b + h]^{i+\frac{1}{2},j} - z_b^{i+\frac{1}{2},j}\right) \quad (31)$$

$$h^{i+\frac{1}{2},j} = \max\left(0, [z_b + h]^{i+\frac{1}{2},j} - z_b^{i+\frac{1}{2},j}\right) \quad (32)$$

The characteristic wave speeds considering wet or dry bed condition are given as (Toro 2002)

$$S^{i+\frac{1}{2},j} = \begin{cases} v_x^{i+\frac{1}{2},j} - 2a^{i+\frac{1}{2},j} & h^{i+\frac{1}{2},j} = 0 \\ \min\left(v_x^{i+\frac{1}{2},j} - a^{i+\frac{1}{2},j}, v_{x,M}^{i+\frac{1}{2},j} - a_M^{i+\frac{1}{2},j}\right) & h^{i+\frac{1}{2},j} > 0 \end{cases} \quad (33)$$

$$S^{i+\frac{1}{2},j} = \begin{cases} u_x^{i+\frac{1}{2},j} + 2a^{i+\frac{1}{2},j} & h^{i+\frac{1}{2},j} = 0 \\ \max\left(v_x^{i+\frac{1}{2},j} + a^{i+\frac{1}{2},j}, v_{x,M}^{i+\frac{1}{2},j} + a_M^{i+\frac{1}{2},j}\right) & h^{i+\frac{1}{2},j} > 0 \end{cases} \quad (34)$$

where

$$a^{i+\frac{1}{2},j} = \sqrt{\hat{g}^{i+\frac{1}{2},j} h^{i+\frac{1}{2},j}} \quad \text{and} \quad a_M^{i+\frac{1}{2},j} = \sqrt{\hat{g}^{i+\frac{1}{2},j} h_M^{i+\frac{1}{2},j}} \quad (35)$$

The velocity and height of debris at the middle region are calculated by

$$v_{x,M}^{i+\frac{1}{2},j} = \frac{1}{2} \left(v_x^{i+\frac{1}{2},j} + v_x^{i+\frac{1}{2},j} \right) + a^{i+\frac{1}{2},j} - a^{i+\frac{1}{2},j} \quad (36)$$

$$h_M^{i+\frac{1}{2},j} = \frac{1}{\hat{g}^{i+\frac{1}{2},j}} \left(\frac{1}{2} \left(a^{i+\frac{1}{2},j} + a^{i+\frac{1}{2},j} \right) + \frac{1}{4} \left(v_x^{i+\frac{1}{2},j} - v_x^{i+\frac{1}{2},j} \right)^2 \right) \quad (37)$$

The gravitational acceleration at a cell face is taken by the linear interpolation as

$$\hat{g}^{i+\frac{1}{2},j} = \frac{1}{2} \left(\hat{g}^{i,j} + \hat{g}^{i+1,j} \right) \quad (38)$$

The conservative variables and advection fluxes at the left and right middle regions are interpolated as

$$U_M^{i+\frac{1}{2},j} = \left(\frac{S^{i+\frac{1}{2},j} - v_x^{i+\frac{1}{2},j}}{S^{i+\frac{1}{2},j} - S_M^{i+\frac{1}{2},j}} \right) \begin{bmatrix} \rho^{i+\frac{1}{2},j} \\ c_s^{i+\frac{1}{2},j} \\ S_M^{i+\frac{1}{2},j} \\ v_y^{i+\frac{1}{2},j} \end{bmatrix} \quad (39)$$

$$\mathbf{F}_M^{i+\frac{1}{2},j} = \mathbf{F}^{i+\frac{1}{2},j} + S^{i+\frac{1}{2},j} \left(\mathbf{U}_M^{i+\frac{1}{2},j} - \mathbf{U}^{i+\frac{1}{2},j} \right) \quad (40)$$

where the middle wave speed $S_M^{i+\frac{1}{2},j}$ is

$$S_M^{i+\frac{1}{2},j} = \frac{S^{i+\frac{1}{2},j} h^{i+\frac{1}{2},j} \left(v_x^{i+\frac{1}{2},j} - S^{i+\frac{1}{2},j} \right) - S^{i+\frac{1}{2},j} h^{i+\frac{1}{2},j} \left(v_x^{i+\frac{1}{2},j} - S^{i+\frac{1}{2},j} \right)}{h^{i+\frac{1}{2},j} \left(v_x^{i+\frac{1}{2},j} - S^{i+\frac{1}{2},j} \right) - h^{i+\frac{1}{2},j} \left(v_x^{i+\frac{1}{2},j} - S^{i+\frac{1}{2},j} \right)} \quad (41)$$

It is noted that $\mathbf{F}_M^{i+\frac{1}{2}\pm,j}$ and $\mathbf{F}^{i+\frac{1}{2}\pm,j}$ in Eq. (40) only contain advection terms of conserved variables. In other words, these parameters do not include the pressure gradient flux parts. Therefore, the pressure gradient flux needs to be separately calculated by using the cell-faced density and height.

$$[\rho\widehat{g}h^2]^{i+\frac{1}{2},j} = \rho^{i+\frac{1}{2},j}\widehat{g}^{i+\frac{1}{2},j}\left(h^{i+\frac{1}{2},j}\right)^2 \tag{42}$$

The cell-faced density and height are also calculated from cell-faced conservative variables obtained by Eq. (24).

$$c_s^{i+\frac{1}{2},j} = \frac{\rho_s[hc_s]^{i+\frac{1}{2},j}}{G_s[h\rho]^{i+\frac{1}{2},j} - \rho_s(G_s-1)[hc_s]^{i+\frac{1}{2},j}} \tag{43}$$

$$\rho^{i+\frac{1}{2},j} = \rho_s c_s^{i+\frac{1}{2},j} + \rho_w \left(1 - c_s^{i+\frac{1}{2},j}\right) \tag{44}$$

$$h^{i+\frac{1}{2},j} = \frac{[h\rho]^{i+\frac{1}{2},j}}{\rho^{i+\frac{1}{2},j}} \tag{45}$$

The momentum dissipation fluxes are discretized by two cell-centered values of shear stress and the cell-faced height as

$$\widetilde{\mathbf{S}}_{d,3 \text{ or } 4}^t = \begin{cases} \mathbf{S}_{d,3 \text{ or } 4}^t & \text{for } \sqrt{\left(\widetilde{\mathbf{U}}_3^{t+\Delta t,(0)}\right)^2 + \left(\widetilde{\mathbf{U}}_4^{t+\Delta t,(0)}\right)^2} \geq \Delta t \sqrt{\left(\mathbf{S}_{d,3}^t\right)^2 + \left(\mathbf{S}_{d,4}^t\right)^2} \\ -\frac{1}{\Delta t} \widetilde{\mathbf{U}}_{3 \text{ or } 4}^{t+\Delta t,(0)} & \text{else} \end{cases} \tag{49}$$

$$\mathbf{U}^{t+\Delta t,(0)} = \mathbf{U}^t + \Delta t \frac{\partial \widetilde{\mathbf{U}}^t}{\partial t} = \widetilde{\mathbf{U}}^{t+\Delta t,(0)} + \Delta t \widetilde{\mathbf{S}}_d^t \tag{50}$$

$$\widehat{T}_x^{i\pm\frac{1}{2},j} = \begin{Bmatrix} 0 \\ 0 \\ \frac{1}{2} h^{i\pm 1,j} \left([\mu_{ap} \overline{\gamma}_{xx}]^{i\pm 1,j} + [\mu_{ap} \overline{\gamma}_{xx}]^{i,j} \right) \\ \frac{1}{2} h^{i\pm 1,j} \left([\mu_{ap} \overline{\gamma}_{xy}]^{i\pm 1,j} + [\mu_{ap} \overline{\gamma}_{xy}]^{i,j} \right) \end{Bmatrix} \tag{46}$$

The momentum source term can be simply discretized as

$$[2\overline{p}\partial_x z_b]^{i,j} = \frac{1}{2\Delta x} \left([\rho\widehat{g}h]^{i+\frac{1}{2},j} + [\rho\widehat{g}h]^{i-\frac{1}{2},j} \right) \left(z_b^{i+\frac{1}{2},j} - z_b^{i-\frac{1}{2},j} \right) \tag{47}$$

The time marching of Eq. (23) is carried out by the predictor-corrector scheme for a numerical accuracy. To prevent reversing the flow direction by the drag vector, the predictor and corrector steps are given as follows:

In the predictor step:

$$\widetilde{\mathbf{U}}^{t+\Delta t,(0)} = \mathbf{U}^t + \Delta t \frac{\partial \widetilde{\mathbf{U}}^t}{\partial t} \tag{48}$$

In the corrector step:

$$\widetilde{\mathbf{U}}^{t+\Delta t,(k)} = \mathbf{U}^t + \frac{\Delta t}{2} \left(\frac{\partial \widetilde{\mathbf{U}}^t}{\partial t} + \frac{\partial \widetilde{\mathbf{U}}^{t+\Delta t,(k-1)}}{\partial t} \right) \tag{51}$$

$$\widetilde{\mathbf{S}}_{d,3 \text{ or } 4}^{t+\Delta t,(k-1)} = \begin{cases} \mathbf{S}_{d,3 \text{ or } 4}^{t+\Delta t,(k-1)} & \text{for } \sqrt{\left(\widetilde{\mathbf{U}}_3^{t+\Delta t,(k)}\right)^2 + \left(\widetilde{\mathbf{U}}_4^{t+\Delta t,(k)}\right)^2} \geq \frac{\Delta t}{2} \sqrt{\left(\mathbf{S}_{d,3}^{t+\Delta t,(k-1)}\right)^2 + \left(\mathbf{S}_{d,4}^{t+\Delta t,(k-1)}\right)^2} \\ -\frac{2}{\Delta t} \widetilde{\mathbf{U}}_{3 \text{ or } 4}^{t+\Delta t,(k)} & \text{else} \end{cases} \tag{52}$$

$$\mathbf{U}^{t+\Delta t,(k)} = \widetilde{\mathbf{U}}^{t+\Delta t,(k)} + \frac{\Delta t}{2} \widetilde{\mathbf{S}}_d^{t+\Delta t,(k-1)} \tag{53}$$

in which $\widetilde{\mathbf{S}}_{d,1 \text{ or } 2} = \mathbf{S}_{d,1 \text{ or } 2}$ (54)

$$\frac{\partial \widetilde{\mathbf{U}}}{\partial t} = \frac{\partial \mathbf{U}}{\partial t} - \mathbf{S}_d \tag{55}$$

where k is the number of iterations needed for the corrector step to improve an approximated solution of a time marching problem and is herein set as 1. After finishing the iterations of

the corrector step, the finally corrected vector $\mathbf{U}^{t+\Delta t,(k)}$ becomes a conserved quantities vector $\mathbf{U}^{t+\Delta t}$ at the next time step. Similar to Eqs. (43)–(45), the cell-centered variables of height, density, and velocity at the next time step can be separated from the updated conserved quantities vector. Note that if a numerical scheme is applied that cannot correctly consider a discontinuous solution in the Riemann problem, the mass conservation may be significantly violated during the time marching of our debris flow model. Additionally, our model can capture the evolution of the solid volume fraction during

debris flow, but this study does not focus on the rheological properties that depend on the solid volume fraction. The rheological properties are homogeneous and constant during the simulation in the paper.

The time interval Δt is controlled for numerical stability as

$$\Delta t = \min \left(CFL_a \cdot \frac{\min(\Delta x, \Delta y)}{\sqrt{v_x^2 + v_y^2 + \sqrt{gh}}}, CFL_d \cdot \frac{\min(\Delta x^2, \Delta y^2)\rho}{4\mu} \right) \quad (56)$$

where CFL_a and CFL_d are empirically selected to 0.3 and 0.9 in this study.

Validations

The numerical model proposed in this study is implemented by MATLAB. In this section, three simulations are performed to validate the implemented numerical code. The first simulation is a circular dam-break test of frictionless condition. The second simulation is a dam-break test of non-Newtonian fluid of which the viscosity can follow the Herschel-Bulkley model well. The last one is multiple debris flow with different densities. The test results provide that the implemented code is sufficiently accurate and applicable to simulate the debris flow.

Circular dam-break of frictionless condition

The dam-break test is a famous validation test used to show the shock-capturing capability in numerical modeling (Wang

et al. 2010; Xia et al. 2013; Ginting and Mundani 2019). In this section, we conducted a circular dam-break test to validate the shock-capturing capability and the isotropy of the implemented numerical scheme. The domain ranges from [40m, 40m] with a flat basal surface and is discretized by a resolution of $0.1\text{m} \times 0.1\text{m}$. The cylindrical dam, with a radius of 2.5m and zero thickness, is placed at the center of the domain. The momentum correction factor is set as unity and the viscosity and corresponding basal friction are ignored. The density is set as 1000kg/m^3 .

The inside and outside regions of the dam are initially filled with water of 2.5-m and 0.5-m heights with an at-rest condition as

$$h = \begin{cases} 2.5\text{ m} & \text{for } \sqrt{x^2 + y^2} \leq 2.5 \\ 0.5\text{ m} & \text{else} \end{cases} \quad (57)$$

The simulation is run for $t = 4.7\text{s}$. After breaking the dam, the water column isotropically spreads outward, as shown in Fig. 1. The evolution of the water column in the result is consistent with Ginting and Mundani (2019). The water height and velocity profiles for a centerline at $t=4.7\text{s}$ are also compared with the analytical solution, as shown in Fig. 2. The results are in overall good agreement with the analytical solutions, although small numerical diffusion occurs near the steep gradient region of the solution.

Dam-break of non-Newtonian fluid

This section simulated a dam-break experiment of a non-Newtonian fluid performed by Ancey and Cochard (2009) to

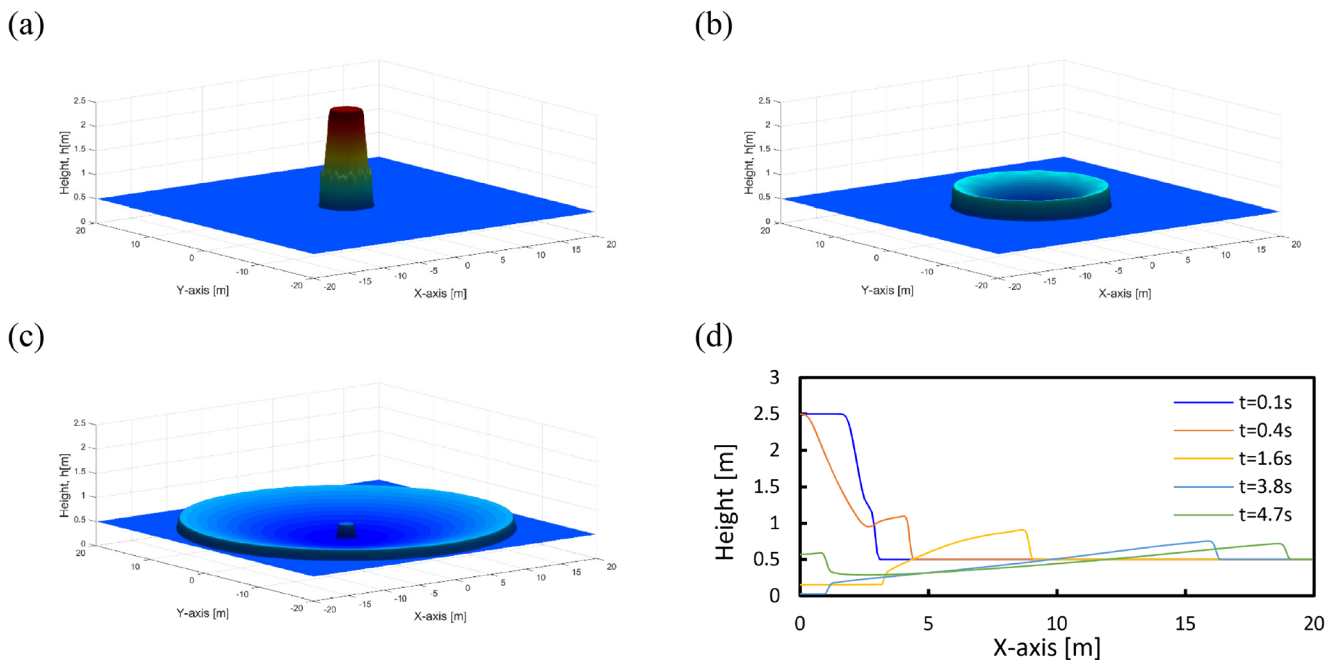


Fig. 1 The configuration of water column after breaking dam $t=0.1\text{s}$ (a), $t=1.6\text{s}$ (b), and $t=4.7\text{s}$ (c). d The water height along the centerline of the domain

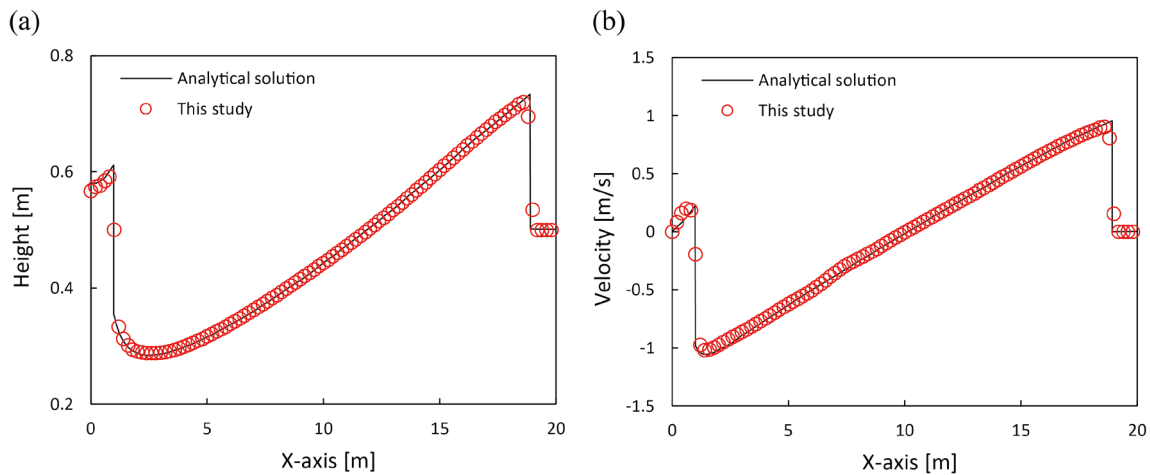


Fig. 2 The water height and velocity along the centerline of the domain at time $t=4.7s$

validate the implemented model. The equipment in Ancy and Cochard (2009) is comprised of a reservoir, a gate, and a plate as shown in Fig. 3. The reservoir size is a width of 0.3m and length of 0.51m. The plate size is a width of 1.6m and a length of 2m. The inclination of equipment is herein set as 12° . In the experiment, the gate was inclined orthogonal to the plate, but this study assumed that the gate was standing in the direction of gravity. The initial height of the fluid at the gate is set as 0.34m. The domain is discretized by a resolution of $0.1m \times 0.1m$. The fluid density is set as $1000kg/m^3$. The rheological parameters of the fluid are $n=0.42$, $k_0=47.68Pa \cdot s^n$, and $\tau_y=89Pa$. The simulation is run for $t=10s$. As similar to the circular dam-break simulation, the gate suddenly disappeared and the stored fluid is accelerated to flow downward. The traveling distance of the fluid front during the simulation was compared to the experimental result and other flow simulations conducted in previous studies as shown in Fig. 3b (Ancy and Cochard 2009; Nikitin et al. 2011; Bernabeu et al. 2014). In the experiment, the initial movement of the fluid ($t < \sim 0.05s$) was much faster than in all simulations, and

the fluid speed decreased sharply afterward. Bernabeu et al. (2014) suspected that this difference could be caused by detailed differences in numerical simulations and experiments. In the early stage, the traveling distance of the fluid front in our simulation was delayed than the experiment but the long-term behavior was in good agreement with the experiment. Therefore, this validation shows that the numerical model developed in this paper is sufficiently accurate to model non-Newtonian fluid behavior for the debris flow.

Multiple debris flow

In this section, the density tracking capability is validated by simulating the merging of multiple debris flow. Figure 4 presents the topology of a simulation domain defined as $100m \times 34m$ that is discretized by a resolution of $0.1m \times 0.1m$. The two U-shaped valleys with an included angle of 30° merge into one at a junction at $x=20m$. The merged valley descends to $x=50m$ with an inclination angle of 15° and then becomes flat. The debris with a radius of 3m and a height of

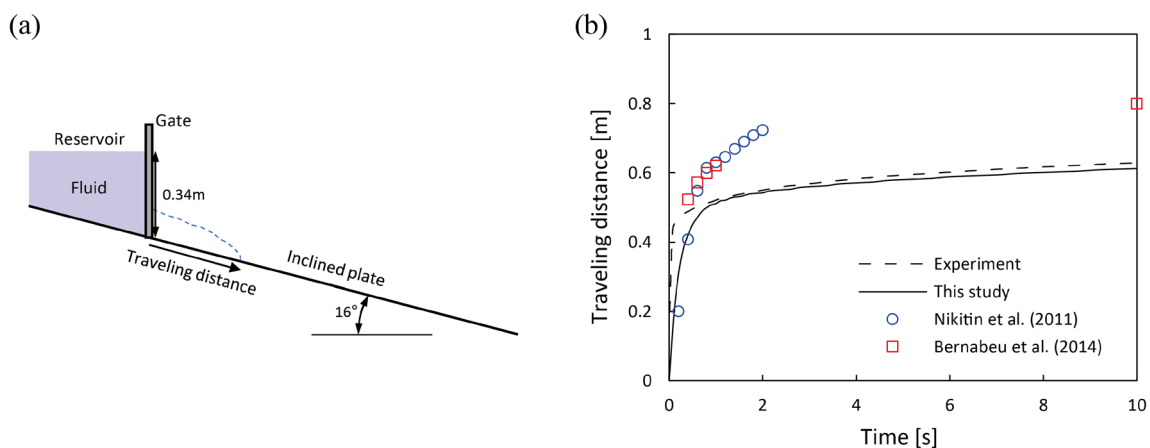


Fig. 3 a Schematic configuration of simulation for the dam-break experiment in Ancy and Cochard (2009). b The traveling distance of the fluid front with time

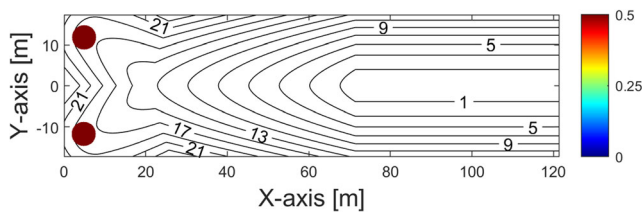


Fig. 4 The topology of multiple debris flow simulation. Initial debris (red circles) with a radius of 3 m and a height of 0.5 m (color bar: debris height (m), contour line: surface level (m))

0.5m is initially placed at the end of the two valleys. The densities of bottom- and top-side debris are 2200 and 1500kg/m³, respectively. The consistency index, flow index, and yield stress in this test are set to 0.3Pa·sⁿ, 0.9, and 100Pa regardless of the debris density. The simulation runs for 12s. Figure 5 displays snapshots of the debris height and density distributions at *t*=2.5, 4.5, 7, and 12s. As debris started to

move, the velocities of the light and heavy debris were similarly developed, but the heavy debris was slightly faster than the light debris.

This result seems to be caused by the differences in debris density. The viscous friction in this study is not a direct function of density. Thus, heavy and light debris under identical conditions lose the same amount of momentums because of the basal friction, and their velocity decreases. However, heavy debris moves relatively faster than the light debris due to its high momentum. The multiple debris flow contacted each other at *t*=3.6 and then advanced side by side. After the contact of two debris flows, the heavy debris wrapped the light debris, as shown in Fig. 5c and d. Due to the momentum of the heavy debris being higher than the light debris, the advancing debris waved to the upside first, then the downside, and then the upside again. Those vestigial movements remain in Fig. 5e–h, and the result is reasonable when considering the inertial effect.

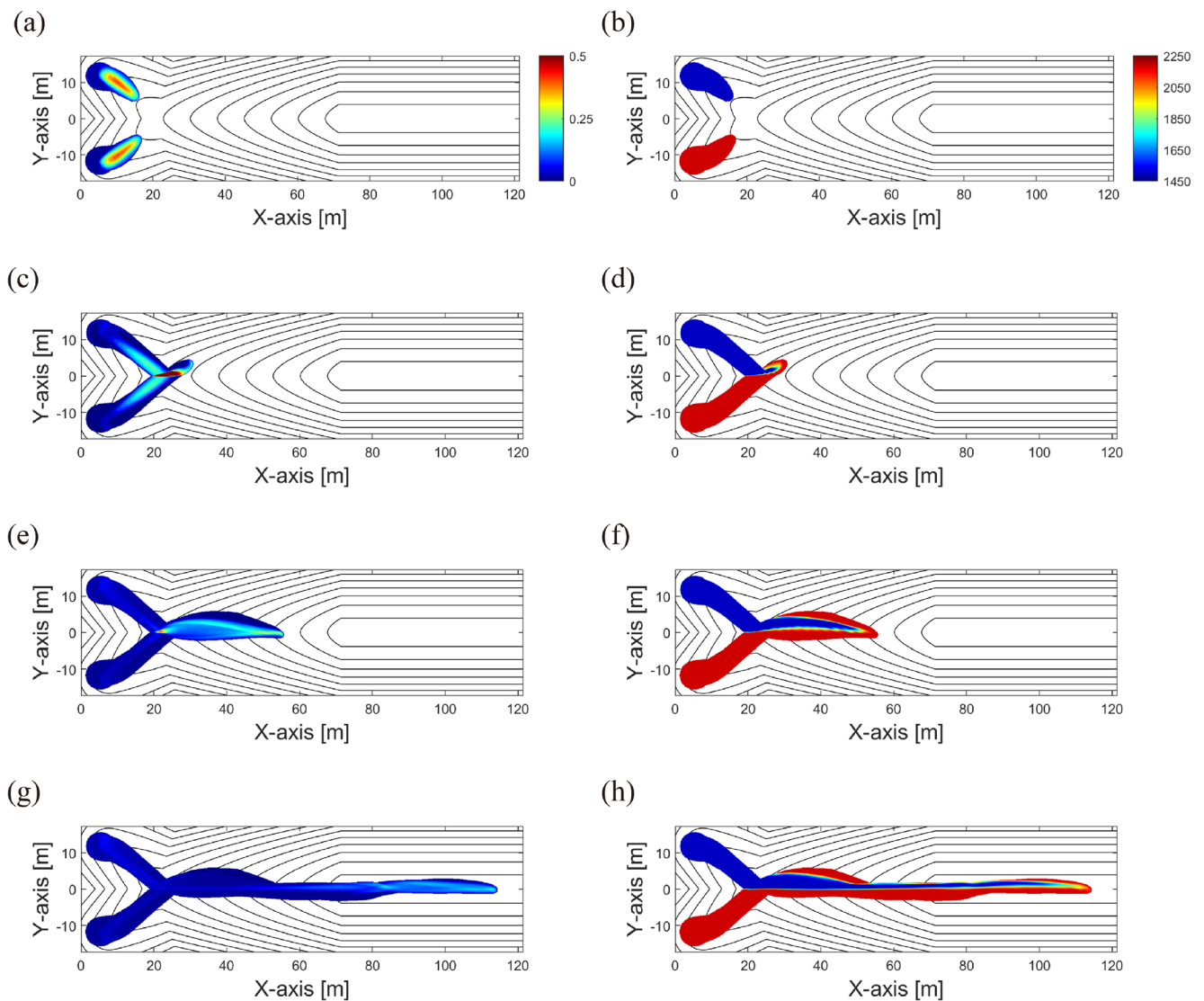


Fig. 5 Snapshots of height (a, c, e, g) and density (b, d, f, h) distributions in multiple debris flow (color bar unit: m (left), kg/m³ (right))

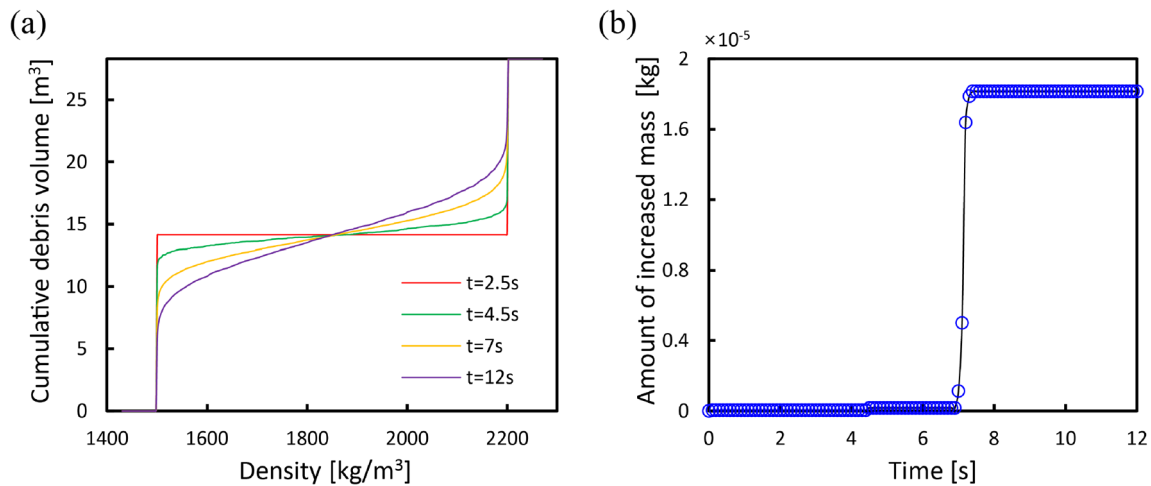


Fig. 6 **a** The debris volume cumulated from low density to high density. **b** Amount of increased mass of the debris

Figure 6a shows the evolution of cumulative debris volume, which is a summation of low-density debris. As time progresses after contact, the portion of intermediate density debris that is in a contact interface with the heavy and light debris increased. The total volume remains conserved in Fig. 6a. For more clarity in mass conservation, Fig. 6b shows the total mass increase from the initial mass. Although it appears that a sharp increment in total mass occurs at $t = 7\text{ s}$, that is only $\sim 3.5 \times 10^{-8}\%$ of the initial total mass and within a sufficiently tolerable range. Therefore, these results show that the numerical schemes implemented in this paper present mass conservation well and imply that they are sufficiently accurate when considering the numerical stability of the debris flow problem.

Parametric study

This section presents a parametric study of the debris rheology for a large-scale debris flow experiment conducted by Iverson

et al. (2010, 2011) whose team is affiliated with the USGS. Previous numerical studies of that experiment used the Coulomb friction model, so the information on the rheological properties of the debris mixture is not well known. This study performs numerical simulations with various model parameters within the same domain of the experiment to provide an understanding of the debris flow behavior according to the rheological properties. Figure 7a illustrates the side view of the experimental setup, in which the downslope channel has a length of 80 m, a width of 2 m, a slope angle of 31° , and a slope angle of 5° . The computational domain is herein constructed by a spatial discretization of $0.2\text{ m} \times 0.2\text{ m}$, as shown in Fig. 7b. The no-slip boundary is applied to all sidewalls.

The debris, with a volume of 6 m^3 and a density of $2000\text{ kg}/\text{m}^3$, is initially placed in the upside of the head gate in the channel. The basal sediment of 12-cm height covers the bed surface at $x=5.7\text{--}53.5\text{ m}$ with a density of $1665\text{ kg}/\text{m}^3$, a saturation of 0.4, a porosity of 0.45, an internal friction angle of 35° , and no cohesion. The specific gravity of solid particles is

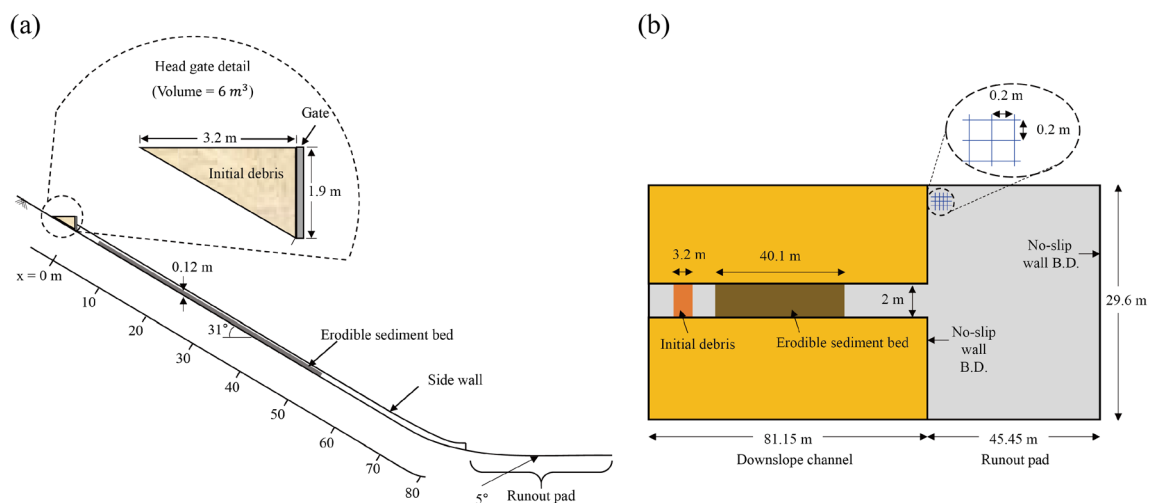


Fig. 7 Schematic configuration of the debris flow domain (adopted from Iverson et al. 2010, 2011)

Table 1 Ranges of input parameters in the parametric study

	Consistency index, k_0 (Pa·s ^{<i>n</i>})	Flow index, <i>n</i>	Yield stress, τ_y (Pa)
Ranges	0.1–100	0.1–1.3	0–800

2.7. The total converted debris volume, including the initial debris and basal sediment, is 13.7m³. A modeling series is run for a simulation time of 50s. The input parameters of the rheological model are systematically varied in predefined ranges of consistency index, flow index, and yield stress, as summarized in Table 1. These ranges were selected by considering previous studies on the rheology of debris (Whipple 1997; Sosio and Crosta 2009; Jeong and Park 2016).

Figure 8 illustrates the traveling distance of the debris flow front from the opened gate for different consistency and flow indices at four different yield stress $\tau_y=0, 100, 400,$ and 800Pa . The semi-transparent yellowish zone covers the range of experimental results in Iverson et al. (2011) and some cases in low- or high-yield stresses were obviously out of the experiment range. For instance, it was observed that the lower the consistency index and the flow index, the more the traveling distance increases. Considering that a frictionless block could

reach on the runout pad at $t \sim 5.7\text{s}$ (Iverson et al. 2011), the debris front movement of low consistency and flow indices at low-yield stress looks faster than the frictionless block. This is because the debris is not only translated by gravity but also spread by a pressure gradient such as a dam-break. As the yield stress increases, the traveling distance and the front speed decrease, and the curves of low consistency index seem to converge to a virtual upper limit. In addition, when the yield stress is 800Pa (Fig. 8d), the debris stops on the channel regardless of the consistency and flow indices, and the flow quickly converged. Thus, we could infer that the curves of the debris with $n=0.1$ and $k_0=0.1\text{Pa}\cdot\text{s}^n$ for four different yield stresses in Fig. 8 are asymptotically close to the upper limit although the debris property may be unrealistic.

To further focus on the effect of flow index on the debris flow, profiles of height, speed, density, and basal shear stress of the debris are displayed for three different flow indices

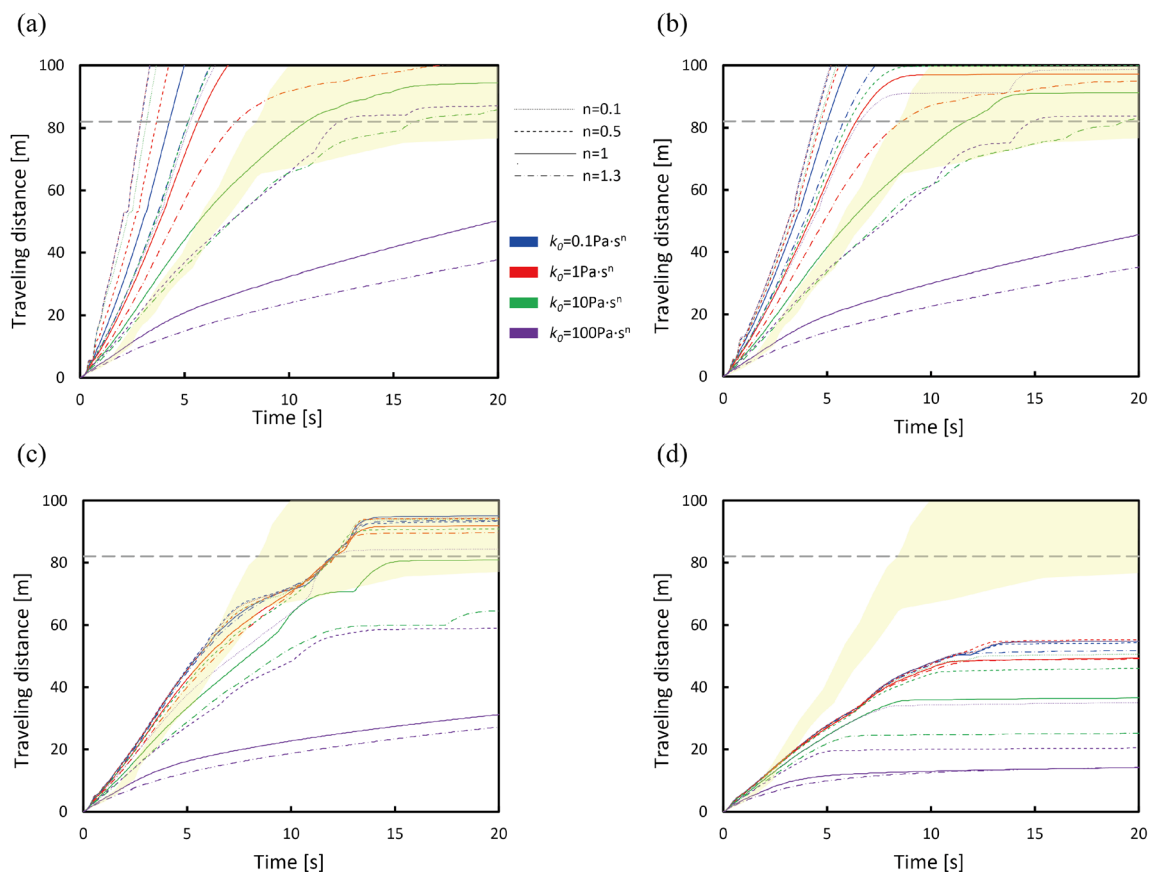


Fig. 8 Traveling distance of debris flow fronts in time for different flow and consistency indices at yield stress $\tau_y = 0$ (a), 100 (b), 400 (c), and 800 Pa (d). The line color and type represent the consistency index and

the flow index, respectively. The gray dashed line indicates the start point of the runout pad. The yellowish zone indicates the range of the USGS experiments (Iverson et al. 2011)

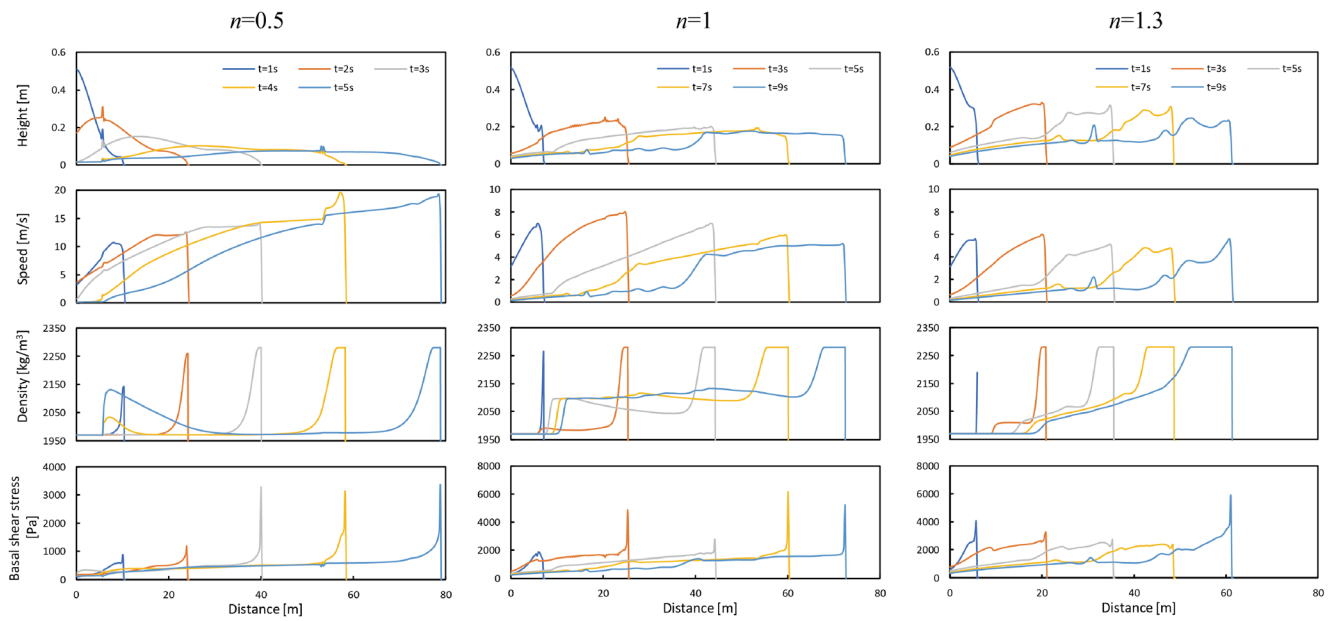


Fig. 9 Profiles of height, speed, density, basal shear stress of the debris for $n=0.5$ (left), 1 (middle), and 1.3 (right) with $k_0 = 10\text{Pa}\cdot\text{s}^n$ and zero yield stress along the midplane of the domain

($n=0.5, 1,$ and 1.3) with a constant consistency index ($k_0=10\text{Pa}\cdot\text{s}^n$) and zero yield stress in Fig. 9. Those profiles were obtained along the midplane of the domain at different

times. The height of the debris front moving along the downslope channel tended to be higher as the flow index was higher. This seems to be caused by two reasons. One is that

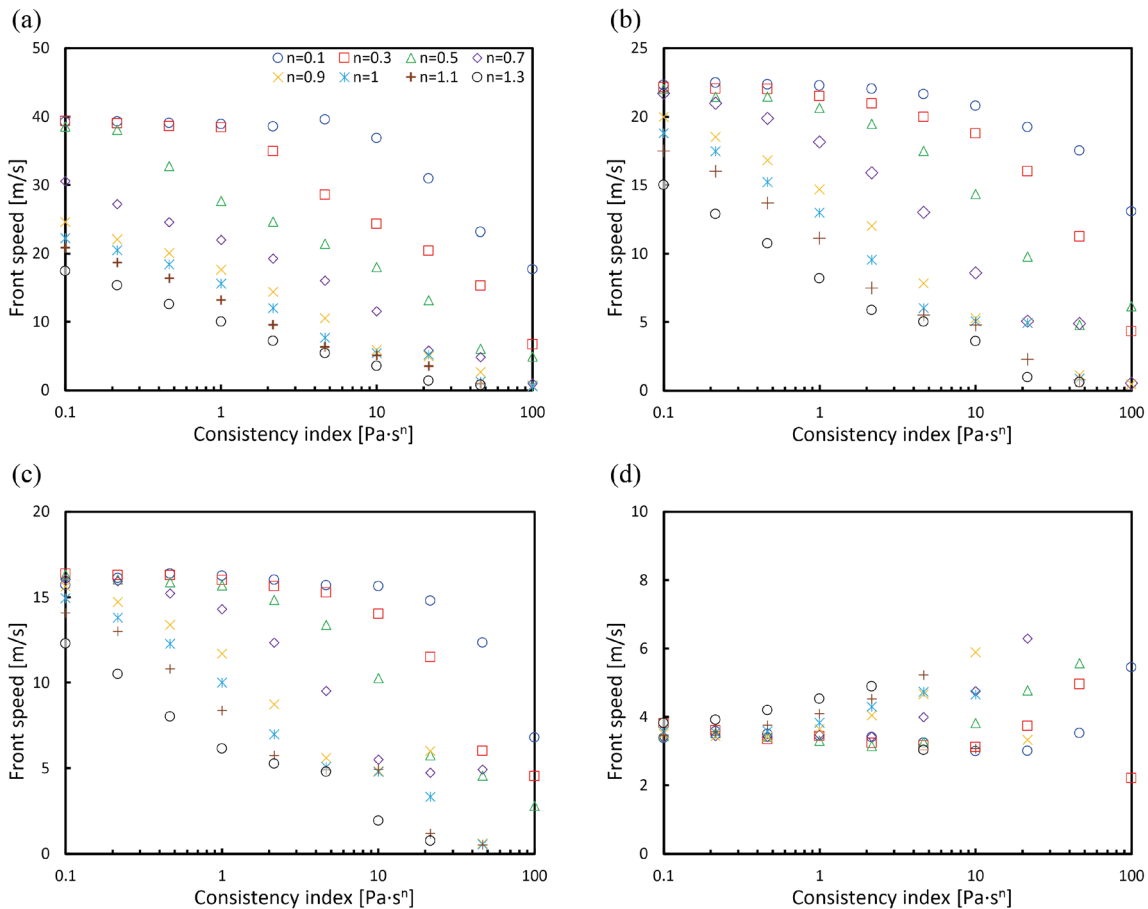


Fig. 10 The averaged front speed at $x=60\text{--}70\text{m}$ for yield stress $\tau_y = 0$ (a), 100 (b), 200 (c), and 400 Pa (d)

the positive feedback owing to the shear-thinning behavior of the debris among low viscosity, high speed (i.e., a high shear rate), and low basal shear stress accelerates spreading the debris front. The other is that the higher basal shear stress and lower speed due to the higher flow index could make greater the entrainment of basal sediment. Note that this study assumes the speed of the debris reduces the erosion rate to the basal sediment according to Eq. (18). The increased density profile can prove that the entrainment predominates in the front of the debris. When entrainment occurs, the debris above the eroded sediment gains in mass but without additional driving momentum, so the debris speed can be reduced or maintained temporarily. Note that this study assumes the debris mixture being saturated. Therefore, the density of the entrained debris mixture is higher than that of the unsaturated basal sediment. Although it seems that the high rate of entrainment causes a rough profile of the debris surface, it may differ from the real profile, because the debris is fully saturated and the turbulence is not considered in this study and because this study does not take into account air entrainment by dilatation and turbulence. As the flow index increases, the entrainment in rear debris may increase, and secondary debris flow may develop. In some of the traveling distance curves in Fig. 8, it is

observed that the debris front slows down for a while and then moves again. This is because the secondary debris flow overtook the slowed debris front and the merged one accelerated again.

Figure 10 presents the averaged front speed of the debris flow at $x=60-70\text{m}$ by calculating the secant gradient of the traveling distance curve at $x=60-70\text{m}$. Note that the measured ranges of averaged speed are 2.4–15m/s in the USGS experiment for post-entrainment flow conditions (Iverson et al. 2011). The front speed in this study increased up to 40m/s as the consistency index and the flow index decreased. In particular, it is observed that the front speed of shear-thinning conditions ($n < 1$) converged to a maximum value when the yield stress τ_y is smaller than 400Pa.

The debris moving through the channel as well as the at-rest debris on the runout pad contains considerable information on rheological behavior. All simulations were run until $t=50\text{s}$, at which point the debris flow could approximately converge to the equilibrium state. Figure 11 illustrates the debris volume on the runout pad at $t=50\text{s}$. There are no data points for the low consistency index and low flow index in Fig. 11 because the debris flow reached the domain boundary of the runout pad before $t=50\text{ s}$, and the simulation stopped.

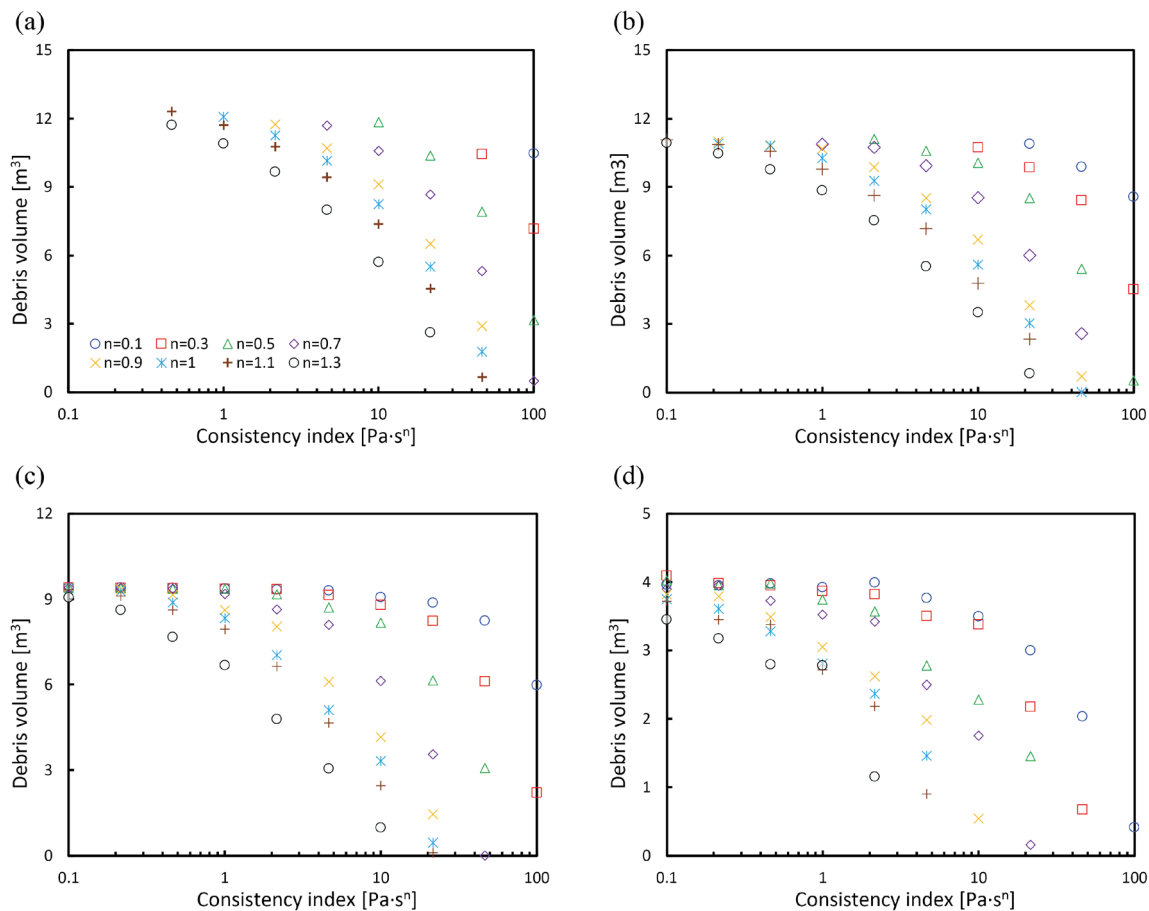


Fig. 11 The debris volume on runout pad at $t=50\text{s}$ for yield stress $\tau_y = 0$ (a), 100 (b), 200 (c), and 400 Pa (d)

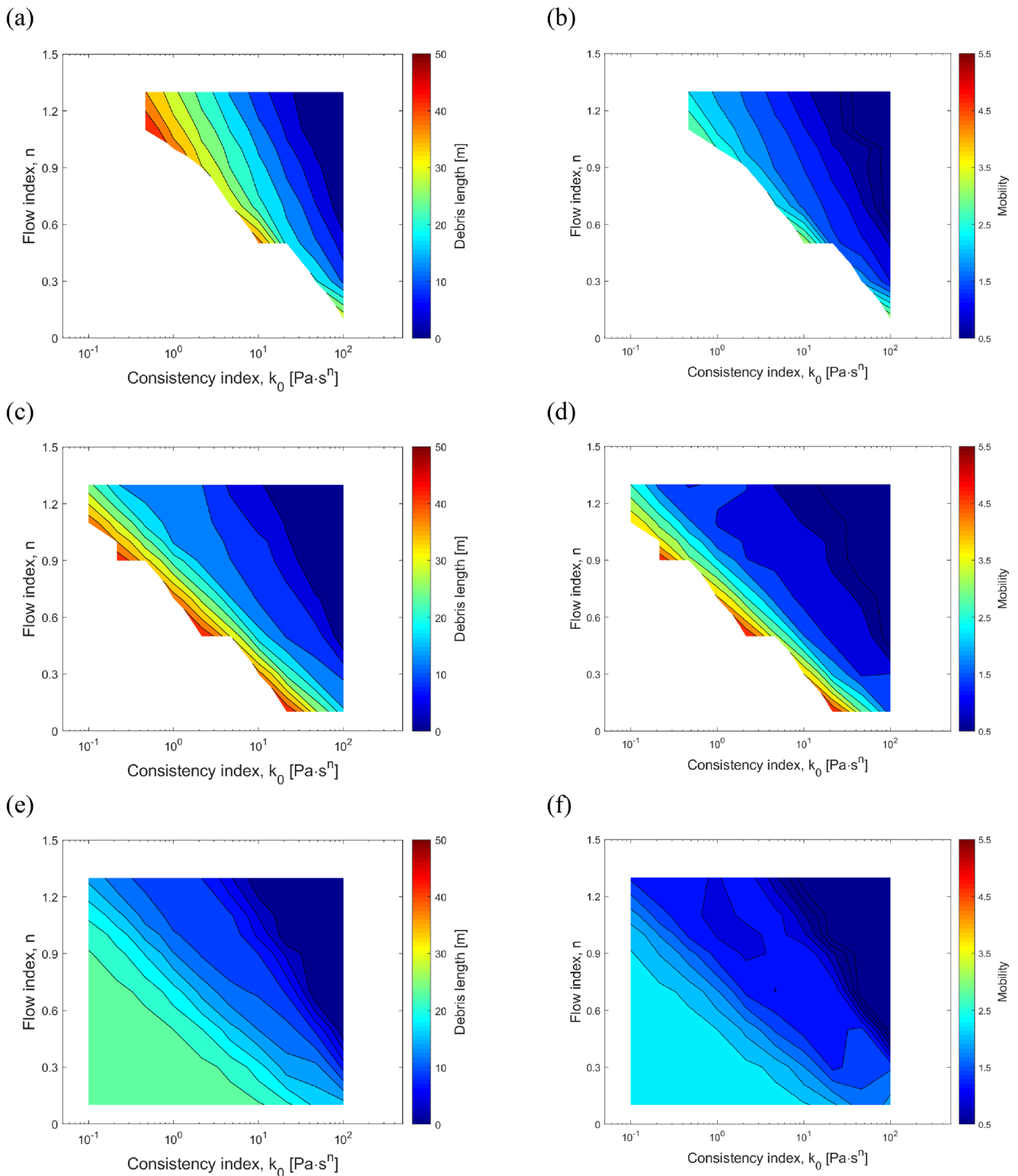


Fig. 12 The debris length on runout pad and corresponding mobility (=length/width) at $t=50$ s for yield stress $\tau_y = 0$ (a, b), 100 (c, d), and 200 Pa (e, f). Un-rendered contour regions in (a)–(d) are that the debris flow reached the domain boundary of the runout pad

As for the consistency index, the flow index and yield stress increased, and the debris volume on the runout pad at $t=50$ s decreased. In particular, the debris flow in all cases for

$\tau_y=800$ Pa does not reach the runout pad at $t=50$ s, and the debris volume for $\tau_y=400$ Pa cases was smaller than the initial debris volume. Because the total debris volume including

basal sediment in this study is smaller than that in the experiment and the debris in the simulation is assumed to be fully saturated, the maximum debris volume on the runout pad in Fig. 11 is also smaller than that in the experiment (8.1–18.3m³) (Iverson et al. 2011). After all simulations, we compared the total mass of debris and basal sediment to the initial total mass. The error was almost $\sim 10^{-8}\%$, which shows that the implemented code well tracks the density evolution by the entrainment and satisfies the mass conservation of the debris flow.

This study also measured the debris length (L) and width (W) on the runout pad at $t = 50$ s and calculated the debris mobility (M) by $M=L/W$. Figure 12 presents the contours mapped to the length (L) and mobility (M) on a consistency index and flow index axes for three different yield stresses ($\tau_y=0, 100, \text{ and } 200\text{Pa}$). The contour regions of the low consistency index, flow index, and yield stress were not rendered because the debris flow reached the domain boundary of the runout pad due to the high flowability and limited domain size. Both the debris length and mobility seem to be inversely proportional to the flow index and the logarithm of the consistency index. For the no-yield stress case ($\tau_y=0\text{Pa}$), the maximum mobility was lower than the case for $\tau_y=100\text{ Pa}$. Additionally, the mobility for $\tau_y=100\text{Pa}$ was higher overall than that for $\tau_y=200\text{Pa}$. This is because the yield stress reduces both the longitudinal advancement of the debris flow and its transversal spreading. In the experiment, the debris length and mobility ranged from 2.5–32.3m and 1.8–2.47, respectively (Iverson et al. 2011). Thus, it appears that the ranges of rheological parameters corresponding to the experiment were more limited for $\tau_y=0\text{--}100\text{Pa}$ than for 200Pa.

Conclusions

This work developed a simplified debris flow model with Herschel-Bulkley rheology for tracking density evolution. A finite volume formulation of the debris flow model was also proposed for accurate and stable numerical simulations. Both the internal and basal frictions of the debris flow were considered in the model as well as the basal topology effect. To verify the numerical accuracy and stability of the proposed method near a shock front, the circular dam-break benchmark was performed, and the result was in good agreement with the analytical solution and showed sufficient isotropy of the solution. The dam-break of non-Newtonian fluid was also simulated, and the result was sufficiently accurate compared to the experiment and other simulations in the previous studies. The multiple debris flow with different densities was also simulated to verify the tracking of density evolution after debris merging. The total debris mass was well conserved in the simulation, and reasonable debris behavior was observed. These validations

indicate that the finite volume schemes implemented in this study are sufficiently appropriate to treat the debris flow model. From the parametric study, the debris behavior depending on various rheological parameters was systematically determined. This could help improve the applicability of the rheology model for debris flow and guide us in determining relevant rheological parameters.

Supplementary Information The online version contains supplementary material available at <https://doi.org/10.1007/s10064-021-02202-9>.

Funding This work was supported by the Basic Science Research Program through the National Research Foundation of Korea (NRF) funded by the Ministry of Education (No. 2018R1A6A1A08025348).

References

- Ancey C, Cochard S (2009) The dam-break problem for Herschel-Bulkley viscoplastic fluids down steep flumes. *J Nonnewton Fluid Mech.* <https://doi.org/10.1016/j.jnnfm.2008.08.008>
- Audusse E, Bouchut F, Bristeau MO et al (2004) A fast and stable well-balanced scheme with hydrostatic reconstruction for shallow water flows. *SIAM J Sci Comput.* <https://doi.org/10.1137/S1064827503431090>
- Bernabeu N, Saramito P, Smutek C (2014) Numerical modeling of non-Newtonian viscoplastic flows: Part II. Viscoplastic fluids and general tridimensional topographies. *Int J Numer Anal Model*
- Chen H, Lee CF (2000) Numerical simulation of debris flows. *Can Geotech J.* <https://doi.org/10.1139/t99-089>
- Crosta GB, Imposimato S, Roddeman D (2009) Numerical modelling of entrainment/deposition in rock and debris-avalanches. *Eng Geol.* <https://doi.org/10.1016/j.enggeo.2008.10.004>
- Fraccarollo L, Capart H (2002) Riemann wave description of erosional dam-break flows. *J Fluid Mech.* <https://doi.org/10.1017/S0022112002008455>
- García-Delgado H, Machuca S, Medina E (2019) Dynamic and geomorphic characterizations of the Mocoa debris flow (March 31, 2017, Putumayo Department, southern Colombia). *Landslides.* <https://doi.org/10.1007/s10346-018-01121-3>
- Ginting BM, Mundani RP (2019) Comparison of shallow water solvers: Applications for dam-break and tsunami cases with reordering strategy for efficient vectorization on modern hardware. *Water (Switzerland).* <https://doi.org/10.3390/w11040639>
- Han Z, Su B, Li Y et al (2019) Numerical simulation of debris-flow behavior based on the SPH method incorporating the Herschel-Bulkley-Papanastasiou rheology model. *Eng Geol.* <https://doi.org/10.1016/j.enggeo.2019.04.013>
- Hong M, Jeong S, Kim J (2019) A combined method for modeling the triggering and propagation of debris flows. *Landslides.* <https://doi.org/10.1007/s10346-019-01294-5>
- Hou J, Wang T, Li P et al (2018) An implicit friction source term treatment for overland flow simulation using shallow water flow model. *J Hydrol.* <https://doi.org/10.1016/j.jhydrol.2018.07.027>
- Hürlimann M, Rickenmann D, Medina V, Bateman A (2008) Evaluation of approaches to calculate debris-flow parameters for hazard assessment. *Eng Geol.* <https://doi.org/10.1016/j.enggeo.2008.03.012>
- Hutter K, Greve R (1993) Two-dimensional similarity solutions for finite-mass granular avalanches with Coulomb- and viscous-type frictional resistance. *J Glaciol.* <https://doi.org/10.3189/s0022143000016026>
- Hutter K, Wang Y, Pudasaini SP (2005) The Savage-Hutter avalanche model: How far can it be pushed? In: *Philosophical Transactions of*

- the Royal Society A: Mathematical, Physical and Engineering Sciences
- Iverson RM (1997) The physics of debris flows. *Rev Geophys.* <https://doi.org/10.1029/97RG00426>
- Iverson RM (2003) The debris-flow rheology myth. In: International Conference on Debris-Flow Hazards Mitigation: Mechanics, Prediction, and Assessment, Proceedings
- Iverson RM, George DL (2014) A depth-averaged debris-flow model that includes the effects of evolving dilatancy. I. Physical basis. *Proc R Soc A Math Phys Eng Sci.* <https://doi.org/10.1098/rspa.2013.0819>
- Iverson RM, Logan M, LaHusen RG, Berti M (2010) The perfect debris flow? Aggregated results from 28 large-scale experiments. *J Geophys Res.* <https://doi.org/10.1029/2009jf001514>
- Iverson RM, Reid ME, Logan M et al (2011) Positive feedback and momentum growth during debris-flow entrainment of wet bed sediment. *Nat Geosci.* <https://doi.org/10.1038/ngeo1040>
- Jeong SW, Park SS (2016) On the viscous resistance of marine sediments for estimating their strength and flow characteristics. *Geosci J.* <https://doi.org/10.1007/s12303-015-0032-3>
- Jeong S, Kim Y, Lee JK, Kim J (2015) The 27 July 2011 debris flows at Umyeonsan, Seoul, Korea. *Landslides.* <https://doi.org/10.1007/s10346-015-0595-0>
- Johnson CG, Kokelaar BP, Iverson RM et al (2012) Grain-size segregation and levee formation in geophysical mass flows. *J Geophys Res Earth Surf.* <https://doi.org/10.1029/2011JF002185>
- Kaitna R, Rickenmann D, Schatzmann M (2007) Experimental study on rheologic behaviour of debris flow material. *Acta Geotech.* <https://doi.org/10.1007/s11440-007-0026-z>
- Laigle D, Coussot P (1997) Numerical modeling of mudflows. *J Hydraul Eng.* [https://doi.org/10.1061/\(ASCE\)0733-9429\(1997\)123:7\(617](https://doi.org/10.1061/(ASCE)0733-9429(1997)123:7(617)
- Li J, Cao Z, Hu K et al (2018) A depth-averaged two-phase model for debris flows over erodible beds. *Earth Surf Process Landforms.* <https://doi.org/10.1002/esp.4283>
- Liu W, He S, Li X, Xu Q (2016) Two-dimensional landslide dynamic simulation based on a velocity-weakening friction law. *Landslides.* <https://doi.org/10.1007/s10346-015-0632-z>
- Mangeney A, Bouchut F, Thomas N et al (2007) Numerical modeling of self-channeling granular flows and of their levee-channel deposits. *J Geophys Res Earth Surf.* <https://doi.org/10.1029/2006JF000469>
- Medina V, Hürlimann M, Bateman A (2008) Application of FLATModel, a 2D finite volume code, to debris flows in the north-eastern part of the Iberian Peninsula. *Landslides.* <https://doi.org/10.1007/s10346-007-0102-3>
- Nikitin KD, Olshanskii MA, Terekhov KM, Vassilevski YV (2011) A numerical method for the simulation of free surface flows of viscoplastic fluid in 3D. *J Comput Math.* <https://doi.org/10.4208/jcm.1109-m11si01>
- Parsons JD, Whipple KX, Simoni A (2001) Experimental study of the grain flow, fluid-mud transition in Debris flows. *J Geol.* <https://doi.org/10.1086/320798>
- Pastor M, Yague A, Stickle MM et al (2018) A two-phase SPH model for debris flow propagation. *Int J Numer Anal Methods Geomech.* <https://doi.org/10.1002/nag.2748>
- Pellegrino AM, Schippa L (2018) A laboratory experience on the effect of grains concentration and coarse sediment on the rheology of natural debris-flows. *Environ Earth Sci.* <https://doi.org/10.1007/s12665-018-7934-0>
- Pellegrino AM, Di Santolo AS, Schippa L (2016) The sphere drag rheometer: A new instrument for analysing mud and debris flow materials. *Int J GEOMATE.* <https://doi.org/10.21660/2016.25.5389>
- Pouliquen O, Forterre Y (2002) Friction law for dense granular flows: Application to the motion of a mass down a rough inclined plane. *J Fluid Mech.* <https://doi.org/10.1017/S0022112001006796>
- Pudasaini SP (2012) A general two-phase debris flow model. *J Geophys Res Earth Surf.* <https://doi.org/10.1029/2011JF002186>
- Savage SB, Hutter K (1989) The motion of a finite mass of granular material down a rough incline. *J Fluid Mech.* <https://doi.org/10.1017/S0022112089000340>
- Schatzmann M, Bezzola GR, Minor HE et al (2009) Rheometry for large-particulated fluids: Analysis of the ball measuring system and comparison to debris flow rheometry. *Rheol Acta.* <https://doi.org/10.1007/s00397-009-0364-x>
- Scotto Di Santolo A, Pellegrino AM, Evangelista A (2010) Experimental study on the rheological behaviour of debris flow. *Nat Hazards Earth Syst Sci.* <https://doi.org/10.5194/nhess-10-2507-2010>
- Sosio R, Crosta GB (2009) Rheology of concentrated granular suspensions and possible implications for debris flow modeling. *Water Resour Res.* <https://doi.org/10.1029/2008WR006920>
- Toro EF (2002) Shock capturing methods for free-surface shallow flows. *Shock methods Free shallow flows*
- Vardoulakis I (2000) Catastrophic landslides due to frictional heating of the failure plane. *Mech Cohesive-Frictional Mater.* [https://doi.org/10.1002/1099-1484\(200008\)5:6<443::AID-CFM104>3.0.CO;2-W](https://doi.org/10.1002/1099-1484(200008)5:6<443::AID-CFM104>3.0.CO;2-W)
- Wang X, Morgenstern NR, Chan DH (2010) A model for geotechnical analysis of flow slides and debris flows. *Can Geotech J.* <https://doi.org/10.1139/T10-039>
- Wang W, Chen G, Han Z et al (2016) 3D numerical simulation of debris-flow motion using SPH method incorporating non-Newtonian fluid behavior. *Nat Hazards.* <https://doi.org/10.1007/s11069-016-2171-x>
- Whipple KX (1997) Open-channel flow of Bingham fluids: Applications in debris-flow research. *J Geol.* <https://doi.org/10.1086/515916>
- Won S, Lee SW, Paik J et al (2016) Analysis of erosion in debris flow experiment using terrestrial LiDAR. *Journal of the Korean Society of Surveying, Geodesy, Photogrammetry and Cartography.* <https://doi.org/10.7848/ksgpc.2016.34.3.309>
- Xia X, Liang Q (2018) A new depth-averaged model for flow-like landslides over complex terrains with curvatures and steep slopes. *Eng Geol.* <https://doi.org/10.1016/j.enggeo.2018.01.011>
- Xia X, Liang Q, Pastor M et al (2013) Balancing the source terms in a SPH model for solving the shallow water equations. *Adv Water Resour.* <https://doi.org/10.1016/j.advwatres.2013.05.004>
- Xia X, Liang Q, Ming X, Hou J (2017) An efficient and stable hydrodynamic model with novel source term discretization schemes for overland flow and flood simulations. *Water Resour Res.* <https://doi.org/10.1002/2016WR020055>
- Yavari-Ramshe S, Ataie-Ashtiani B, Sanders BF (2015) A robust finite volume model to simulate granular flows. *Comput Geotech.* <https://doi.org/10.1016/j.compgeo.2015.01.015>
- Zanuttigh B, Lamberti A (2004) Analysis of debris wave development with one-dimensional shallow-water equations. *J Hydraul Eng.* [https://doi.org/10.1061/\(ASCE\)0733-9429\(2004\)130:4\(293](https://doi.org/10.1061/(ASCE)0733-9429(2004)130:4(293)